

Electronic Supplementary Information

for

Work Function and Temperature Dependence of Electron Tunneling through an N-Type Perylene Diimide Molecular Junction with Isocyanide Surface Linkers

Christopher E. Smith,^{†‡} Zuoti Xie,^{‡*} Ioan Bâldea,^{§*} and C. Daniel Frisbie^{‡*}

[†]Department of Chemistry and [‡]Department of Chemical Engineering and Materials Science, University of Minnesota, Minneapolis, Minnesota 55455

[§]Theoretische Chemie, Universität Heidelberg, INF 229, D-69120 Heidelberg, Germany and National Institute of Lasers, Plasmas and Radiation Physics, Institute of Space Science, POB MG-23 RO 077125, Bucharest, Romania.

*To whom correspondence should be addressed

E-mail: zxie@umn.edu, ioan.baldea@pci.uni-heidelberg.de, frisbie@umn.edu

Table of Contents

Synthesis of CN₂PDI

Figure S1. Infrared spectroscopy and UV-vis absorption of CN₂PDI precursors and SAM

X-ray Photoelectron Spectroscopy

Figure S2. High resolution X-ray photoelectron spectroscopy (HRXPS) of C, N and O in CN₂PDI SAMS

Table S1. Component of C, N, O of CN₂PDI on Ag, Au, and Pt substrate obtained from high resolution XPS and length of PDI obtained by angle resolved XPS.

Figure S3. Angle resolved XPS spectra of CN₂PDI on Ag, Au and Pt substrates.

Voltammetry

Figure S4. Cyclic Voltammetry and surface coverage of CN₂PDI SAMs

Conducting Probe Atomic Force Microscopy

Figure S5. Linear average *I-V* curves of Ag/Ag, Au/Ag, Ag/Pt, Au/Au, Au/Pt and Pt/Pt junctions

Figure S6. Transition Voltage Spectroscopy plots of $\text{abs}(I^2/V)$ versus $1/V$

Figure S7. Single level model simulation of temperature dependent Pt/Pt junction *I-V* curves.

Theory

Temperature Dependence of the Low Bias Resistance. Equations S1-S6

Results for the Two-Step Model, Equations S7-S9

Figure S8. Single-step model vs two-step model

Synthesis of CN₂PDI and precursors

2,9-Bis-(4-amino-2,3,5,6-tetramethylphenyl)anthra[2,1,9-def;6,5,10-d'e'f']diisoquinolin-1,3,8,10-tetraone (2). Perylene-3,4:9,10-tetracarboxylic bisanhydride (7g, 12 mmol) was added to imidazole (93g, 1.37 mol), tetramethylphenylenediamine (15.95g, 97 mmol) and zinc acetate (2.2 g, 12 mmol) under nitrogen. The mixture was heated to 100 C until imidazole melted. The purple melt was stirred until the materials were dissolved then heated at 160°C for 3 h. The solution was poured into 300 mL of 2 M HCl and the precipitate was filtered and washed with 500 mL water followed by 100 mL ethanol then 50 mL pentane. The dark maroon solid was dried at 100 mTorr and 60°C for 2h. Yield 9.36 g (88%) dark maroon solid, mp >300 °C; R_f (silica gel, CHCl₃) 0.6; UV/vis (DMSO) λ_{max} = 427.6 (0.08), 457.5 (0.28), 488.2 (0.65), 525.2 nm (1.00); ¹HNMR (DMSO-d₆) δ 8.61 (d, 8.1 Hz, 4 H), 8.4 (d, 7.8 Hz, 4 H), 4.61 (d, 2 H), 2.28 (s, 12 H), 2.01 (s, 12 H) ppm. HRMS (FAB+, C₄₄H₃₆N₄O₄) calcd m/z 685.2828 (M+1), found m/z 685.2808 (M+1), Δ = ± 0.0020.

2,9-Bis-(4-formamido-2,3,5,6-tetramethylphenyl)anthra[2,1,9-def;6,5,10-d'e'f']diisoquinolin-1,3,8,10-tetraone (3). Acetic formic anhydride was made *in situ* by adding acetic anhydride (3.7 mL, 40 mmol) to formic acid (3 mL, 80 mmol) and heated at 60°C for 2.5 h while stirring. To this solution was added **2** (200 mg, 0.4 mmol) dispersed in the minimum amount of CH₂Cl₂ (2 mL), followed by an additional 3 mL of formic acid. The dark purple solution was stirred under nitrogen for 24 h. The reaction was removed from heat and the volatiles were reduced at 80 mtorr and 90°C for 1 h. The dark maroon solid was washed with pentane then purified by column chromatography on silica gel with 2:1 CH₂Cl₂:MeOH as the eluent to yield 0.245 g (48%), mp>300°C; R_f (silica gel, 2:1 CH₂Cl₂:MeOH) 0.8; UV/vis (DMSO) λ_{max} = 431.1 (0.06), 458.1 (0.24), 489.2 (0.66), 525.9 nm (1.00); ¹HNMR (DMSO-d₆) δ 9.65 (s, 2 H), 9.49 (s, 2H), 8.80 (d, 8.4 Hz, 4 H), 8.51 (d, 7.7 Hz, 4 H), 2.14 (s, 12 H), 2.00 (s, 12 H) ppm. HRMS (FAB+, C₄₄H₃₆N₄O₄) calcd m/z 741.2635 (M+1), found m/z 741.2625 (M+1), Δ = ± 0.0010.

2,9-Bis-(4-isocyano-2,3,5,6-tetramethylphenyl)anthra[2,1,9-def;6,5,10-d'e'f']diisoquinolin-1,3,8,10-tetraone (4). Triethylamine (0.238 mL) and **3** (241 mg) were dispersed in 10 mL of CH₂Cl₂ under nitrogen. Phosphorous oxychloride 9μL (mM) was added dropwise, then the slurry was allowed to react for 2h in absence of oxygen and under a gentle flow of nitrogen. The slurry

was filtered and rinsed with CH_2Cl_2 (100 mL). The filtrate was washed with sodium bicarbonate and water, then extracted with CH_2Cl_2 and dried over sodium sulfate. The solvent was reduced and the product was purified with column chromatography in silica gel with CH_2Cl_2 as the eluent to yield 51 mg (18%). R_f (silica gel, CH_2Cl_2) 0.26; UV/vis (DMSO) λ_{max} = 432.0 (0.14), 463.0 (0.39), 494.0 (0.84), 531.1 nm (1.00); ^1H NMR (DMSO- d_6) δ 8.880 (m, 4 H), 2.47 (s, 12 H), 2.10 (s, 12 H) ppm. HRMS (FAB+, $\text{C}_{44}\text{H}_{36}\text{N}_4\text{O}_4$) calcd m/z 704.2423, found m/z 704.2395 (M+1), $\Delta = \pm 0.0028$.

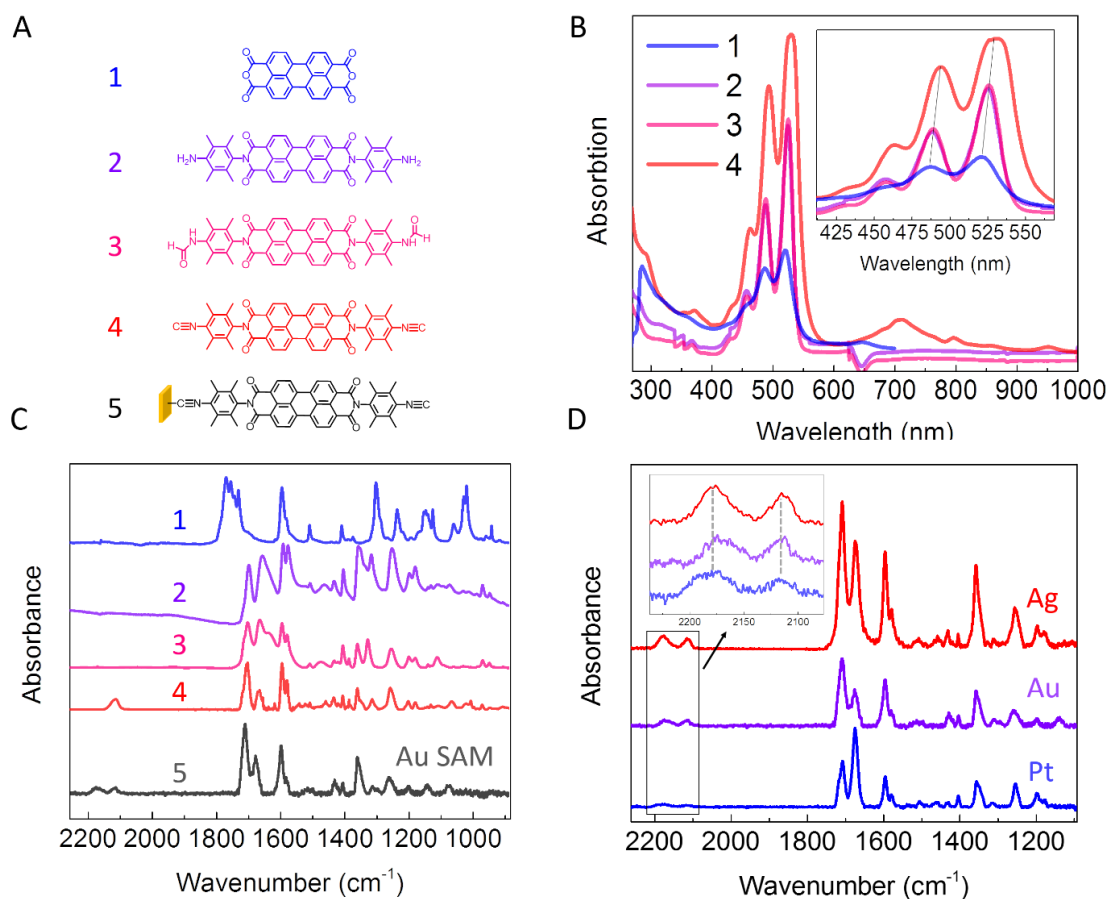


Figure S1. (A) Structures of the three precursors and CN_2PDI . (B) UV-vis of the three precursors (1-3) and CN_2PDI (4) in DMSO. (C) Infrared spectra (KBr, 32 scans at resolution 2 cm^{-1}) of 1-4 and RAIRS of CN_2PDI SAM on gold surface (5, 400 scans at resolution 2 cm^{-1}). (D) RAIRS of CN_2PDI SAMs on Ag, Au and Pt surfaces (400 scans at resolution 2 cm^{-1}).

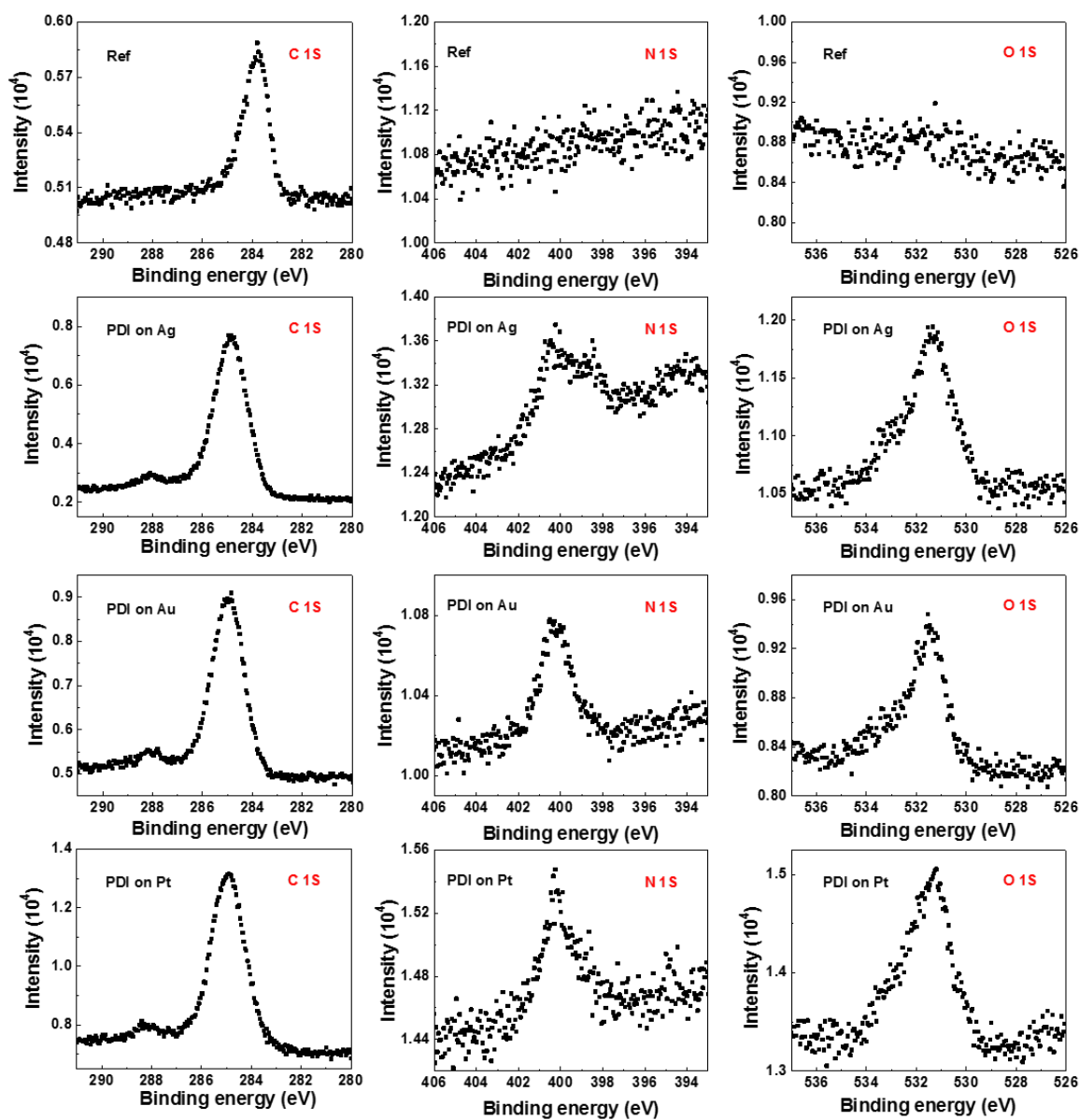
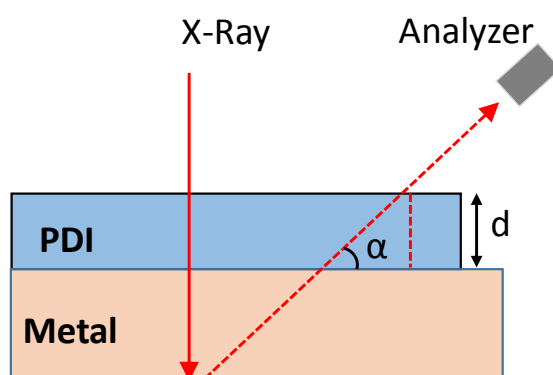


Figure S2. XPS of carbon, nitrogen and oxygen in CN₂PDI SAMs (bottom nine plots) on Ag, Au and Pt. A bare Au surface (top three plots) was immediately measured as a reference after thermal evaporation. For the spectra of PDI SAMs, the C1s peak at 288 eV is due to the CO and NC moieties.

Table S1. Summary of XPS results. The theoretical thickness of a PDI SAM is 2.43 nm, which equals the PDI molecular length, normal to the substrate, plus one metal-C bond of 0.19 nm.¹

		Theoretical	Ag	Au	Pt
Atomic Components	C	82	80	82	82
	N	9	10	8	7
	O	9	10	10	11
ARXPS	SAM Thickness		1.91±0.1	1.88±0.1	1.85±0.2
	Molecular Tilt angle		38°	39°	40°

Angle resolved XPS



Scheme S1. Angle resolved XPS

If photoelectrons are collected at certain angles with respect to the surface, the emission path lengths in the film are increased by a factor of $\sin\alpha$, as can be seen in Scheme S1. The XPS signal attenuation is expressed as

$$I = I_0 e^{-d/\lambda \sin\alpha}$$

where I_0 is the photoelectron intensity from the bare substrate, I is the intensity from PDI covered samples, d is the thickness of the PDI monolayer, λ is the attenuation length, α is the angle between the surface and analyzer axis (take-off angle). Here we collected Ag 3d, Au 4f and Pt 4f photoelectrons as a function of take-off angles set to 20°, 30°, 40°, 50°, 60°, 70°, 80° and 90°, Figure S3. The reported attenuation lengths for Ag 3d and Au 4f photoelectrons in organic SAMs are 3.6 nm and 4.2 nm, respectively.² Because $\lambda \propto \sqrt{E}$, where E is the photoelectron

kinetic energy, and because the Pt 4f core level binding energy is only slightly smaller than Au 4f core level binding energy, and therefore the E values will be similar, we assume the attenuation length for Pt 4f is also close to 4.2 nm. Using the formula for I above, we calculated d , the SAM thickness, for the different samples, Table S1. The SAM thicknesses listed in Table S1 are the averages from the eight different take-off angles.

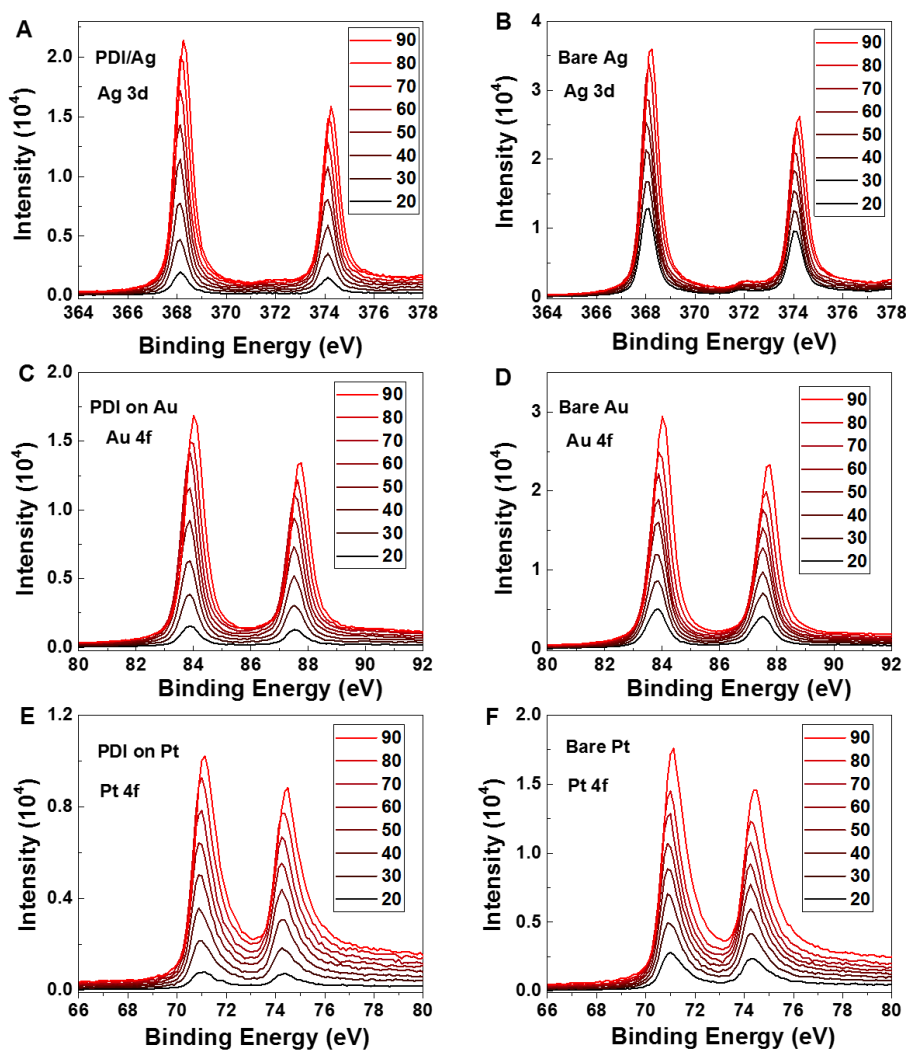


Figure S3. Angle resolved XPS spectra of (A) Ag 3d for CN₂PDI on Ag, (B) Ag 3d of bare Ag, (C) Au 4f for CN₂PDI on Au, (D) Au 4f of bare Au, (E) Pt 4f for CN₂PDI on Pt and (F) Pt 4f of bare Pt.

Voltammetry methods. Cyclic square wave voltammograms of CN₂PDI were taken in a 3-neck cell with an Au disc electrode, Pt wire and Ag wire as the working, counter and reference electrodes, respectively. The electrolyte was 0.1 M TBAPF₆ in degassed DMSO. All sweeps started at 0 V with respect to Ag wire and proceeded toward negative potential (red arrow) then cycled back to 0 V. Potentials shown are referenced to an internal Fc/Fc⁺ redox couple. There are two very characteristic one-electronic redox events for the CN₂PDI in DMSO solution. Pulsed-wave voltammetry, such as cyclic square wave voltammetry (CSWV), is much more sensitive to faradaic current at the working electrode interface and afforded well resolved PDI redox peaks for CN₂PDI SAMs as shown in Figure S3B. For CSWV the AC component amplitude and sampling width were set to 25 mV and 1 ms, respectively, and the sweep rate was varied by changing the period and increment of the DC sweep. Regular cyclic voltammetry of CN₂PDI SAMs is shown in Figure S3C. The most pronounced reverse sweep oxidation peaks (O1 and O2) in the Figure S3C voltammograms were used to calculate the CN₂PDI surface coverage in molecules/nm² according to,

$$\text{surface coverage} = \frac{Q}{nFA}$$

where Q is the charge injected into the molecular wires, n is the number of electrons involved in the electron-transfer process, F is the Faraday constant, and A is the surface area of the sample exposed to the electrolyte (in this case $\sim 0.78 \text{ cm}^2$). The charge injected was determined by integrating the first oxidation peak O1 in the current versus time voltammogram for each sweep rate. The coverage was 0.8 ± 0.3 molecules/nm² calculated from the 250 mV/s scan rate.

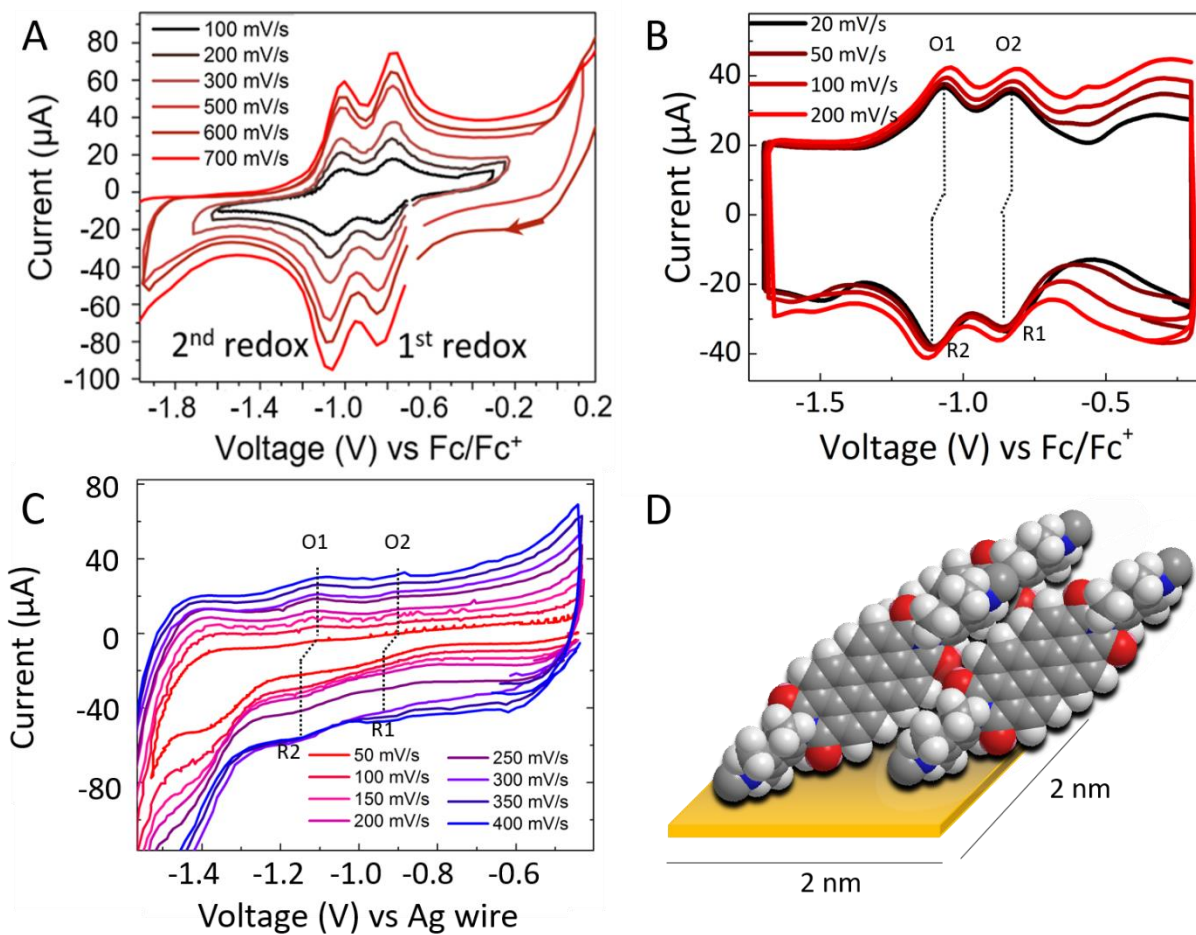


Figure S4. (A) Cyclic voltammograms for ~1 mM CN₂PDI in DMSO. (B) Cyclic square wave voltammograms of a CN₂PDI SAM on a Au surface. (C) Cyclic voltammograms of a CN₂PDI SAM on a Au surface. (D) Schematic representing ~0.8 PDIs/nm² (~3.2 PDI per 4 nm²)

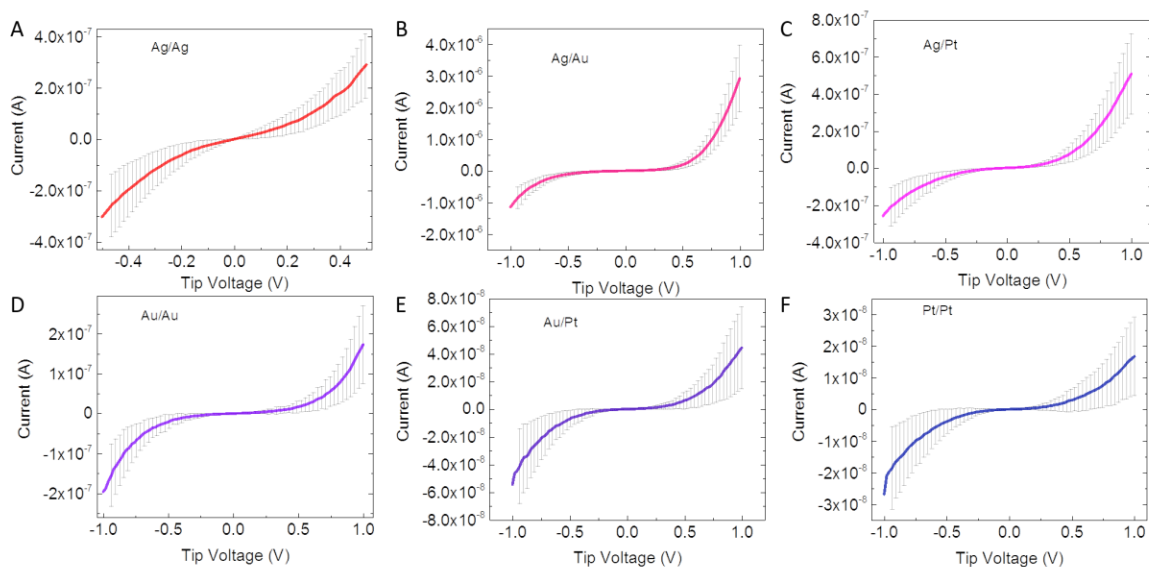


Figure S5. (A-F) Average I - V curves for different metal contacts from Figure 5 on a linear scale. The colored lines represent the average of ~ 150 traces over 4 spots on the sample and the grey error bars show the standard deviation σ . All I - V curves are included in the averaging with no data selection.

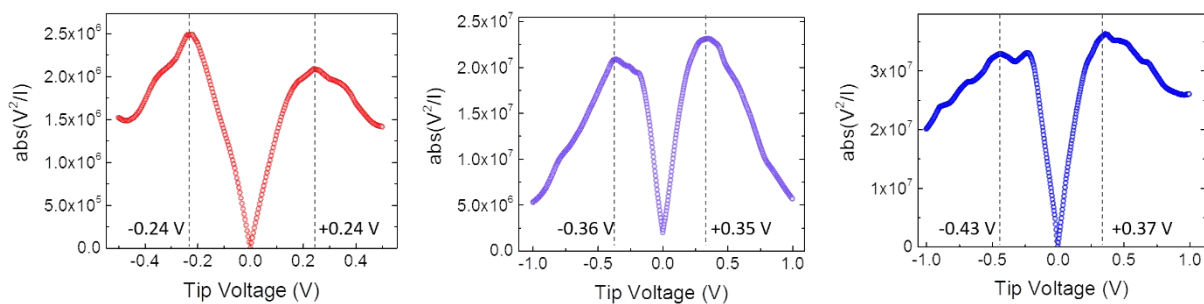


Figure S6. Average TVS curves for junctions with Ag/Ag (left), Au/Au (center) and Pt/Pt (right) contacts. Maxima on the curves correspond to V_t^+ and V_t^-

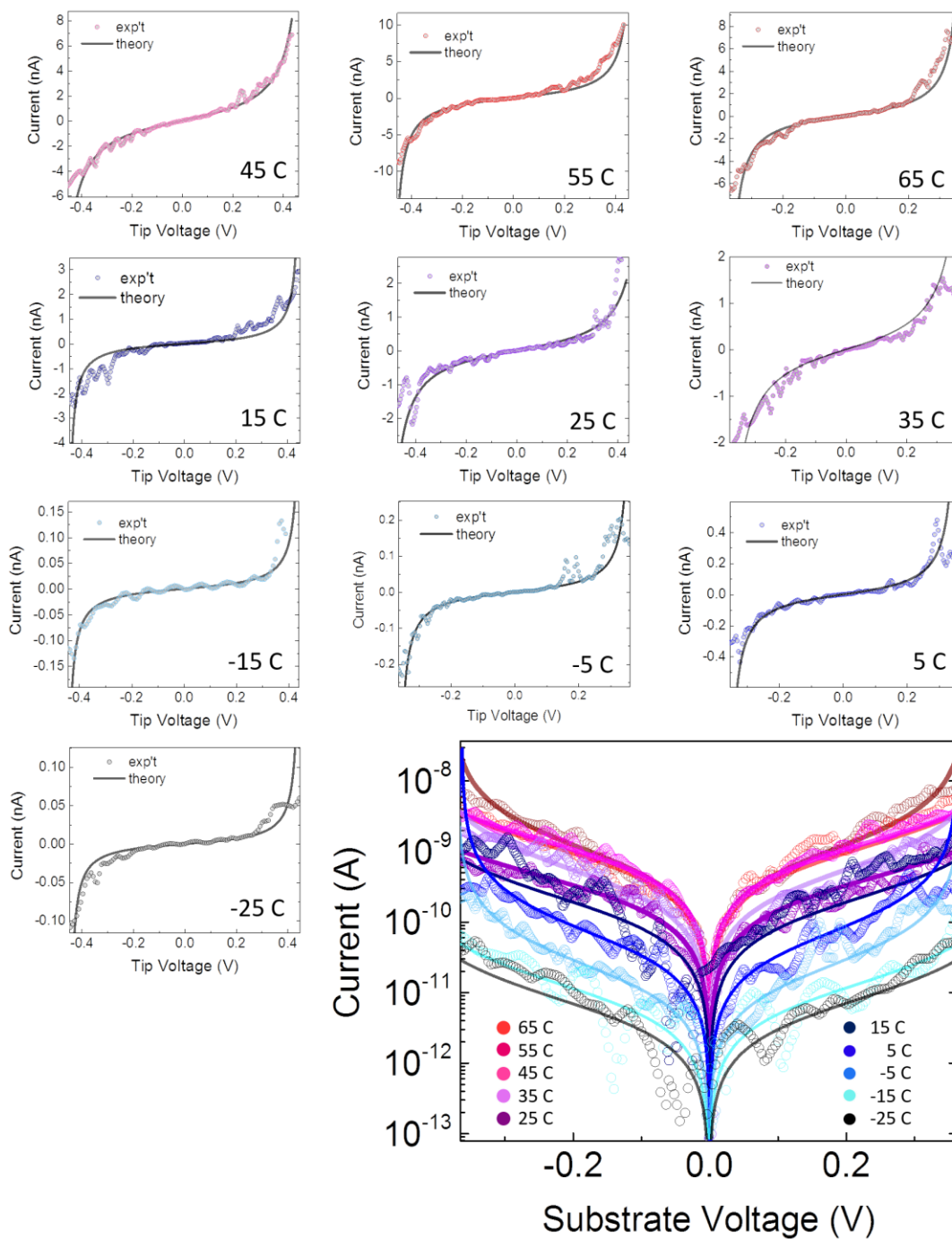


Figure S7. Average I - V curves used to generate the temperature dependent data found in Figure 9. Linear plots of the experimental data (colored circles) were simulated with the single level model (black lines). The bottom right shows a semi log plot of these same average I - V curves.

Temperature Dependence of the Low Bias Resistance

To see that, contrary to what is commonly assumed, a tunneling mechanism does not rule out a substantial temperature dependence of the charge transport, we start from the Landauer formula of the current mediated by a single level (MO) of energy ε_0 .

$$I(V, T) = \frac{2e}{h} \int_{-\infty}^{+\infty} dE \mathbb{T}(E; \varepsilon_0, V) [f(E - eV/2) - f(E + eV/2)] \quad (\text{S1})$$

where \mathbb{T} is the transmission function and

$$f(E) = \frac{1}{1 + \exp\left(\frac{E}{k_B T}\right)}$$

is the Fermi distribution function of energy E measured with respect to the equilibrium Fermi energy set to zero for convenience ($E_F = 0$). The low bias conductance

$$G(T) \equiv \left. \frac{\partial}{\partial V} I(V, T) \right|_{V \rightarrow 0} \quad (\text{S2})$$

can be easily obtained from Eq. S1 to be of the form

$$\frac{G(T)}{G_0} = \frac{1}{4k_B T} \int_{-\infty}^{+\infty} dE \mathbb{T}(E; \varepsilon_0, V = 0) \operatorname{sech}^2\left(\frac{E}{2k_B T}\right) \quad (\text{S3})$$

where G_0 is the conductance quantum. Importantly, the hyperbolic secant function sech entering Eq S3 results from taking the derivative of the electrodes' Fermi distributions; it is solely the result of the thermal broadening in electrodes. In cases where the level width Γ is sufficiently smaller than the thermal energy $k_B T$ and the thermal energy $k_B T$ is sufficiently smaller than the level offset ε_0 , the integrand in the RHS of Eq S3 possesses two well separated narrow peaks located at $E = \varepsilon_0$ and $E = 0$, respectively, which correspond to the sharp maxima of the two factors of the integrand. On this basis, one can show³ that the conductance can be expressed as

$$\frac{G(T)}{G_0} = \frac{G(T=0)}{G_0} + \frac{\operatorname{const}}{k_B T} \operatorname{sech}^2\left(\frac{\varepsilon_0}{2k_B T}\right) \quad (\text{S4})$$

By inspecting the trend in Figure 9B, one can conclude that the conductance at zero temperature $G(T=0)$ is negligible for the presently investigated CP-AFM junctions. So, we can neglect the first term in the RHS of Eq S4 for the presently considered junctions and thus get the following temperature dependence of the low bias resistance $R \equiv 1/G$

$$R(T) \approx \operatorname{const} \times k_B T \cosh^2\left(\frac{\varepsilon_0}{2k_B T}\right) \quad (\text{S5})$$

which coincides with Eq. 6 used in the main text. Here $\cosh(x) = (e^x + e^{-x})/2$ is the hyperbolic cosine. Noticing that $\cosh^2(x/2) \approx e^x/4$ for $x \gg 2$, for MO energy offsets much larger than the thermal energy ($|\varepsilon_0| \gg 2k_B T$), Eq. S5 yields

$$R(T) \approx \text{const} \times k_B T \exp\left(\frac{\varepsilon_0}{k_B T}\right) \quad (\text{S6})$$

In such cases, Eq S6 basically describes a thermally activated Arrhenius dependence with an activation energy equal to the MO energy offset $|\varepsilon_0|$. For LUMO-mediated transport (as the case of the junctions considered in this paper) $\varepsilon_0 = \varepsilon_l > 0$; for HOMO-mediated transport, $\varepsilon_0 = \varepsilon_h < 0$.

Results for the Two-Step Model

Based on results valid in the more general case of gated molecular junctions,^{4,5} in the parameter range of interest for the present analysis, the current via a two-step electron transfer through a molecule characterized by the reorganization energy λ can be expressed as

$$I \approx I_0 V \exp[-(\lambda - e|V|)/(4k_B T)] \quad (\text{S7})$$

where I_0 is a constant. In the limit $V \rightarrow 0$ in the above equation yields the zero-bias conductance

$$G = [I/V]_{V \rightarrow 0} = I_0 \exp[-\lambda/(4k_B T)] \sim \exp[-E_a/(k_B T)] \quad (\text{S8})$$

Eq. S8 describes an Arrhenius behavior of the conductance with an activation energy $E_a = 4\lambda$, as expressed by eq. 12 in the main text. By combining eqs. S7 and S8 one gets

$$I = GV \exp[e|V|/(4k_B T)] \quad (\text{S9})$$

which coincides with eq. 10 of the main text. By imposing the condition expressed by eq. 6 of the main text

$$dI/dV|_{V=V_t} = 2 I/V|_{V=V_t}$$

using the current given by eq. S9 one immediately obtains the transition voltage V_t having the form

$$eV_t = 4k_B T$$

that is, eq. 13 of the main text.

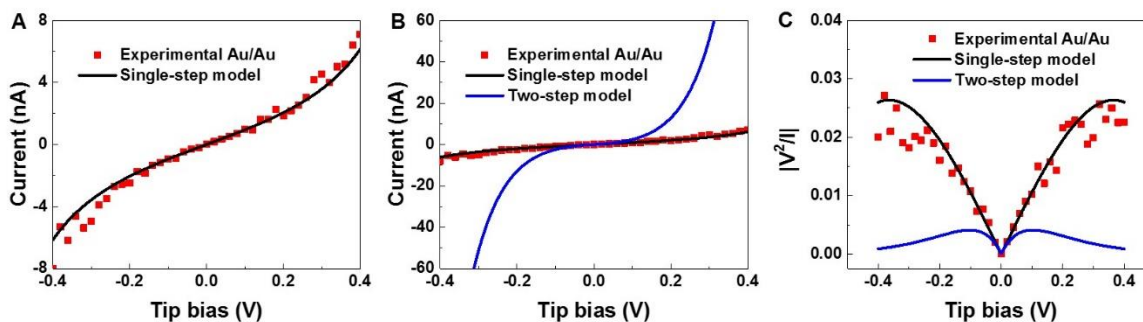


Figure S8. A raw I - V curve (red points) measured for a CN₂PDI junctions with gold electrodes fitted with the single-step model (eq. 3, of the main text; black curve in panel a) and with the two-step model (eq. 10 of the main text; blue curve in panel b). The transition voltage spectra $V^2/|I|$ vs. V corresponding to the experimental data (red points), single-step model (black curve), and two-step model (blue curve) are depicted in panel c.

References

- 1 V. Huc, J. Bourgoin, C. Bureau, G. Zalczer and S. Palacin, *J. Phys. Chem. B*, 1999, **103**, 10489–10495.
- 2 P. E. . Laibinis, C. D. . Bain and G. M. Whitesides, *J. Phys. Chem.*, 1991, **95**, 7017–7021.
- 3 I. Bâldea, *Phys. Chem. Chem. Phys.*, 2017, **19**, 11759–11770.
- 4 I. G. Medvedev, *Phys. Rev. B*, 2007, **76**, 125132.
- 5 I. Bâldea, *J. Phys. Chem. C*, 2013, **117**, 25798–25804.